

**Local and nonlocal electron-phonon couplings in K<sub>3</sub> picene and the effect of metallic screening**

Michele Casula, Matteo Calandra, and Francesco Mauri

*CNRS and Institut de Minéralogie et de Physique des Milieux Condensés, Université Pierre et Marie Curie, Case 115,  
4 Place Jussieu, 75252, Paris Cedex 05, France*

(Received 21 June 2012; published 20 August 2012)

We analyze the properties of electron-phonon couplings in K<sub>3</sub> picene by exploiting a molecular-orbital representation derived in the maximally localized Wannier function formalism. This allows us to go beyond the analysis done in *Phys. Rev. Lett.* **107**, 137006 (2011), and separate not only the intra- and intermolecular phonon contributions but also the local and nonlocal electronic states in the electron-phonon matrix elements. Despite the molecular nature of the crystal, we find that the purely molecular contributions (Holstein-like couplings where the local deformation potential is coupled to intramolecular phonons) account for only 20% of the total electron-phonon interaction  $\lambda$ . In particular, the Holstein-like contributions to  $\lambda$  in K<sub>3</sub> picene are four times smaller than those computed for an isolated neutral molecule, as they are strongly screened by the metallic bands of the doped crystal. Our findings invalidate the use of molecular electron-phonon calculations to estimate the total electron-phonon coupling in metallic picene, and possibly in other doped metallic molecular crystals. The major contribution (80%) to  $\lambda$  in K<sub>3</sub> picene comes from nonlocal couplings due to phonon-modulated hoppings. We show that the crystal geometry together with the molecular picene structure leads to a strong one-dimensional spatial anisotropy of the nonlocal couplings. Finally, based on the parameters derived from our density-functional theory calculations, we propose a lattice modelization of the electron-phonon couplings in K<sub>3</sub> picene which gives 90% of *ab initio*  $\lambda$ .

DOI: [10.1103/PhysRevB.86.075445](https://doi.org/10.1103/PhysRevB.86.075445)

PACS number(s): 31.15.A–, 74.70.Kn, 63.20.kd

**I. INTRODUCTION**

Understanding the transport properties of molecular crystals based on hydrocarbon molecules is relevant not only to fundamental condensed matter physics, but also for applications in nanoelectronics. For instance, organic field-effect transistors are appealing as they are flexible, lightweight, and cheap. Rubrene-based field-effect transistors<sup>1,2</sup> display tunable mobilities that can be as large as 40 cm<sup>2</sup>/(V s). More recently it was shown that picene field-effect transistors<sup>3</sup> based on liquid electrolytes have *p*-channel characteristics,<sup>4</sup> although with much reduced mobilities with respect to rubrene.

Transport properties of organic molecular crystals can also be tuned by intercalation of alkali or alkaline earth metals. K intercalation leads to metallic states in phthalocyanine materials<sup>5</sup> and in several other polycyclic aromatic hydrocarbons. In picene,<sup>6</sup> phenanthrene,<sup>7,8</sup> coronene,<sup>9</sup> and in 1,2:8,9-dibenzopentacene,<sup>10</sup> intercalation stabilizes a superconducting state with critical temperatures ( $T_c$ ) up to 33 K. A detailed understanding of transport phenomena in such systems is then relevant also for the realm of fundamental research.

An important source of intrinsic scattering in aromatic molecular crystals is provided by the electron-phonon coupling. In these systems there is an interplay between intramolecular local interactions and intermolecular nonlocal interactions. Determining the mutual role of local and nonlocal interactions is hardly doable without a proper theoretical approach. Molecular crystals can indeed behave very differently, depending on the details of the molecules composing the crystal and on their arrangement. In alkali-doped fullerenes,<sup>11</sup> superconductivity is supposed to be mostly due to intramolecular phonons. In this case, if the electronic states coupled to the phonons are molecular and the metallic screening is weak, then the problem can be tackled at a molecular level by the

calculation of electron-phonon interaction<sup>12,13</sup> on an isolated ionized molecule.

The situation is more complicated in the field of hydrocarbon molecular crystals. In the case of K<sub>3</sub> picene, molecular calculations<sup>14</sup> using the B3LYP functional give a large electron-phonon coupling that alone can almost explain  $T_c$ . However, the generalization of this approach to other hydrocarbon molecular crystals predicts a decrease of the critical temperature with the increase of the molecular size, in disagreement with experimental data.<sup>6–8,10</sup> Indeed, in experimentation the largest  $T_c$  is for the crystal composed by the largest molecules. Subedi and Boeri<sup>15</sup> performed density-functional-theory (DFT) calculations in which the crystal structure of pristine picene was adopted and K doping was treated in a rigid doping approach. The screening of the self-consistent potential was assumed to be that of insulating picene. A very large electron-phonon coupling was found mostly due to intramolecular phonons, in agreement with Ref. 14.

In our previous work<sup>16</sup> we performed DFT calculations, relying on fewer approximations than in Ref. 15. The theoretically devised crystal structure of K<sub>3</sub> picene was considered<sup>16,17</sup> and K atoms were explicitly included in the calculation. Furthermore, we included the metallic screening of crystalline K<sub>3</sub> picene in the self-consistent potential. By projecting the phonon polarizations into intramolecular and intermolecular vibrations, we found that K<sub>3</sub> picene has a strong electron-phonon coupling ( $\lambda = 0.73$ ) that is partially due to the coupling to intermolecular and intercalant phonons (40%) and partially to the coupling to intramolecular phonons (60%), in disagreement with Refs. 14 and 15. In our present work, we go beyond what we have done in Ref. 16. Instead of analyzing the “locality” of the electron-phonon coupling in terms of phonon projections only, we study it also by means

of electronic projections onto a molecular basis, which allows one to distinguish between the on-site electronic Hamiltonian and the hopping parts, both modulated by the coupling with phonons. This approach leads to a stricter distinction between purely molecular and crystal contributions, and yields a further reduction of the purely molecular component, estimated to be about 20% of the total  $\lambda$ .

The three approaches illustrated above, namely, molecular calculations, rigid doping of the crystal, and explicit treatment of the dopants, rely on different approximations that could explain the discrepancies. An important one is the treatment of the electronic screening and its effects on the electron-phonon interaction. In molecular calculations<sup>14</sup> and in Ref. 15, metallic screening is neglected. Analogy with alkali-doped fullerenes points out, however, that this assumption is not necessary fulfilled. In  $K_3C_{60}$ , it has been suggested that metallic screening strongly affects the electron-phonon coupling.<sup>18–20</sup> For example,  $A_{1g}$  modes causing a shift without splitting of the  $t_{1u}$   $C_{60}$  molecular levels, are supposed to be screened by the charge transfer from up-shifted to down-shifted levels,<sup>20</sup> i.e., by the metallic screening in the solid. In  $K_3$  picene the situation could be similar. However, the relative contribution of intramolecular, intermolecular, and intercalant interactions remains unclear and largely unexplored. In this work we carry out a detailed and quantitative analysis of the total electron-phonon coupling  $\lambda$  in  $K_3$  picene by addressing these issues.

The paper is organized as follows. In Sec. II we provide the general definition of local and nonlocal electron-phonon couplings for a molecular crystal. In Sec. III we describe the geometry of  $K_3$  picene, and we show the dominant hoppings of the corresponding tight-binding Hamiltonian in the Wannier basis. In Sec. IV electron-phonon calculations are carried out by discriminating between local and nonlocal couplings. We find that the purely local contributions account for only 20% of the full  $\lambda$ , while the remaining part comes from nonlocal sources. Section V analyzes the screening acting on the local electron-phonon terms by a direct comparison between the crystal and the isolated (unscreened) molecule. We show that the effect of the metallic screening provided by the crystal environment to the deformation potential is sizable, with a strong reduction of the local electron-phonon coupling with respect to the corresponding strength found in the neutral isolated molecule. In Sec. VI we look for the most important nonlocal terms contributing to the total  $\lambda$  and we build a model Hamiltonian with a few nonlocal electron-phonon couplings added to the local part, which gives 90% of the total  $\lambda$ . The conclusions are in Sec. VII.

## II. DEFINITION OF LOCAL AND NONLOCAL ELECTRON-PHONON COUPLINGS IN A MOLECULAR CRYSTAL

We suppose that the band structure of a molecular crystal is described by the electronic tight-binding Hamiltonian  $H_{el}$ , written in a basis set built out of molecular orbitals  $|i, m\rangle = c_{im}^\dagger |0\rangle$ , where  $i$  is the index of the molecular site having its center of mass located at the equilibrium position  $\mathbf{R}_i$ , and  $m$  is the orbital index, with  $c_{im}^\dagger$  and  $c_{jn}$  satisfying canonical anticommutation relations. For simplicity, we assume here that

there is only one molecule per unit cell, so the vectors  $\mathbf{R}_i$  define also the Bravais lattice.  $H_{el}$  reads then as

$$H_{el} = - \sum_{ij} \sum_{mn} t_{mn}(\mathbf{R}_j - \mathbf{R}_i) c_{im}^\dagger c_{jn}, \quad (1)$$

where we omitted the spin index by implicitly assuming that the spin-up and spin-down components are equivalent, namely, there is no spin symmetry breaking. The hopping matrix is defined as

$$-t_{mn}(\mathbf{R}_j - \mathbf{R}_i) = \langle i, m | H | j, n \rangle, \quad (2)$$

where we exploit the lattice translational invariance.

In second quantization a phonon displacement  $\mathbf{u}_s$  of atom  $s$  with mass  $M_s$  relative to the  $i$ th molecule is

$$\mathbf{u}_s(\mathbf{R}_i) = \frac{i}{N_q} \sum_{\mathbf{q}\nu} \frac{1}{\sqrt{2M_s\omega_{\mathbf{q}\nu}}} \mathbf{e}_{\mathbf{q}\nu}^s (b_{\mathbf{q}\nu} + b_{-\mathbf{q}\nu}^\dagger) e^{i\mathbf{q}\cdot\mathbf{R}_i + i\mathbf{q}\cdot\boldsymbol{\tau}_s}, \quad (3)$$

where  $N_q$  is the number of phonon momentum points describing the system,  $\omega_{\mathbf{q}\nu}$  is the phonon dispersion of mode  $\nu$  at a given momentum  $\mathbf{q}$ ,  $\mathbf{e}_{\mathbf{q}\nu}^s$  is the three-dimensional  $s$ -atomic component of the phonon eigenvector  $\mathbf{e}_{\mathbf{q}\nu}$ , and  $\boldsymbol{\tau}_s$  is the position of the atom  $s$  in the unit cell. The operators  $b_{\mathbf{q}\nu}^\dagger$  and  $b_{\mathbf{q}\nu}$  satisfy canonical bosonic commutation relations.

The harmonic phonon Hamiltonian  $H_{\text{phon}}$  reads as

$$H_{\text{phon}} = \sum_{\mathbf{q}\nu} \omega_{\mathbf{q}\nu} \left( b_{\mathbf{q}\nu}^\dagger b_{\mathbf{q}\nu} + \frac{1}{2} \right). \quad (4)$$

The complete Hamiltonian for the electron-phonon (el-phon) problem includes electron-phonon coupling terms, and is written as

$$H = H_{el} + H_{\text{phon}} + H_{\text{el-phon}}^{\text{local}} + H_{\text{el-phon}}^{\text{nonlocal}}, \quad (5)$$

where the local electron-phonon coupling is

$$H_{\text{el-phon}}^{\text{local}} = \frac{1}{N_q} \sum_{\mathbf{q}\nu} \sum_i \sum_{mn} g_{mn}^{\mathbf{q}\nu}(\mathbf{0}) e^{i\mathbf{q}\cdot\mathbf{R}_i} c_{im}^\dagger c_{in} (b_{-\mathbf{q}\nu}^\dagger + b_{\mathbf{q}\nu}), \quad (6)$$

while the nonlocal coupling  $H_{\text{el-phon}}^{\text{nonlocal}}$  is

$$\frac{1}{N_q} \sum_{\mathbf{q}\nu} \sum_{ij} \sum_{mn} (g_{mn}^{\mathbf{q}\nu}(\mathbf{R}_j - \mathbf{R}_i) e^{i\mathbf{q}\cdot\mathbf{R}_i} c_{im}^\dagger c_{jn} b_{\mathbf{q}\nu} + \text{h.c.}). \quad (7)$$

The phase  $e^{i\mathbf{q}\cdot\mathbf{R}_i}$  makes the total momentum conserved in the electron-phonon scattering terms. The electron-phonon coupling strength projected on the molecular orbitals is defined as

$$g_{mn}^{\mathbf{q}\nu}(\mathbf{R}_j - \mathbf{R}_i) = \sum_s \langle i, m | \frac{\delta v}{\delta \mathbf{u}_{\mathbf{q}s}} | j, n \rangle \cdot \mathbf{e}_{\mathbf{q}\nu}^s / \sqrt{2M_s\omega_{\mathbf{q}\nu}}, \quad (8)$$

where  $i, j$  are indices of molecular sites,  $\mathbf{u}_{\mathbf{q}s}$  is the Fourier transform of the phonon displacement  $\mathbf{u}_s(\mathbf{R}_i)$ , and  $\delta v / \delta \mathbf{u}_{\mathbf{q}s}$  is the (screened) deformation potential.

From Eq. (6), it is apparent that the local coupling is a Holstein-type interaction which couples the phonons with on-site molecular electronic terms, while in Eq. (7) the nonlocal couplings modulate the hoppings  $t_{mn}(\mathbf{R}_j - \mathbf{R}_i)$  in

$H_{el}$  via the bosonic fields  $b_{-q\nu}^\dagger$  and  $b_{q\nu}$ . The local and non-local coupling strengths are proportional to the deformation potential expressed in the molecular-orbital basis, centered on either the same site or two different molecules, respectively. By translational invariance, the strength depends only on the vector  $\mathbf{R}_j - \mathbf{R}_i$ . It is worth pointing out that in this context the definition of “local” and “nonlocal” couplings is purely electronic. In our previous work,<sup>16</sup> we distinguished between the “intermolecular” and “intramolecular” contributions based on the phonon projections. The intramolecular phonons are those having  $\mathbf{e}_{q\nu}$  projected on the single molecule manifold, while the intermolecular phonons are those having  $\mathbf{e}_{q\nu}$  spanned by the rigid molecular rototranslations together with all intercalant displacements. Therefore, one can expand the bosonic fields  $b_{q\nu}$  into  $b_{q\nu}^{\text{inter}} + b_{q\nu}^{\text{intra}}$ , a resolution of the identity being the sum of intermolecular and intramolecular projections. We thus note that cross-contributions such as intramolecular phonons in nonlocal couplings or intermolecular phonons in local couplings are possible. Projection of both the electronic and phononic parts guarantees the isolation of the single-molecule contribution. In this work, we are going to use the words “local” and “nonlocal couplings” to mean the electronic molecular basis set projections as in Eqs. (6) and (7), respectively, while we keep the notation of Ref. 16 by using “intramolecular” and “intermolecular phonons” to refer to the phonon projections.

### III. GEOMETRY AND BAND STRUCTURE OF $K_3$ PICENE

The molecules in the  $K_3$  picene crystal are arranged to satisfy the  $P_1^2$  symmetry group. The unit cell contains two molecules and is monoclinic with axes  $a = 8.707 \text{ \AA}$ ,  $b = 5.912 \text{ \AA}$ ,  $c = 12.97 \text{ \AA}$ ,  $\alpha = 90^\circ$ ,  $\beta = 92.77^\circ$ , and  $\gamma = 90^\circ$ . The unit-cell parameters have been taken from the

experiment,<sup>6</sup> while the internal coordinates have been optimized after a full geometry relaxation performed in a DFT framework within the local-density approximation (LDA) (for more details see the Supplementary Materials section of Ref. 16). The final structure is drawn in Fig. 1, where we plot the orthogonal projections of the unit cell repeated twice in each crystallographic direction. From Figs. 1(b) and 1(c), one can clearly see the molecular stacking along the  $c$  axis, while in Fig. 1(a) (the  $ab$  projection) the molecular herringbone arrangement of each layer is visible. The intercalant occupies the interstitial space and tunes the intermolecular angles by steric effect.

In order to understand the interplay between the  $K_3$  picene geometry and its band structure, we are going to derive a tight-binding model constructed on a Wannier function basis. The maximally localized Wannier representation of the DFT orbitals is useful not only to implement an interpolation scheme for computing the band structure and the electron-phonon matrix elements, but also to have a physical insight on the system. For example, the formation of the chemical bond in a solid can be visualized by means of the Wannier representation of the molecular orbitals (MOs). In a molecular crystal, as the picene, the Wannier representation is even more natural, as it builds on the local nature of molecular sites, where the MOs are strongly localized. The spatial local representation given by the Wannier transformation helps in modeling the electronic structure of the  $K$ -doped picene and understanding the mechanism which sets the superconductivity.

By following Ref. 22, the maximally localized Wannier functions (MLWFs) are defined as

$$\tilde{w}_{n\mathbf{R}}(\mathbf{r}) = \frac{1}{\sqrt{N_w}} \sum_{\mathbf{k}} \left[ \sum_m U_{mn}^{\text{MLWF}}(\mathbf{k}) \psi_{m\mathbf{k}}(\mathbf{r}) \right] e^{-i\mathbf{k}\cdot\mathbf{R}}, \quad (9)$$

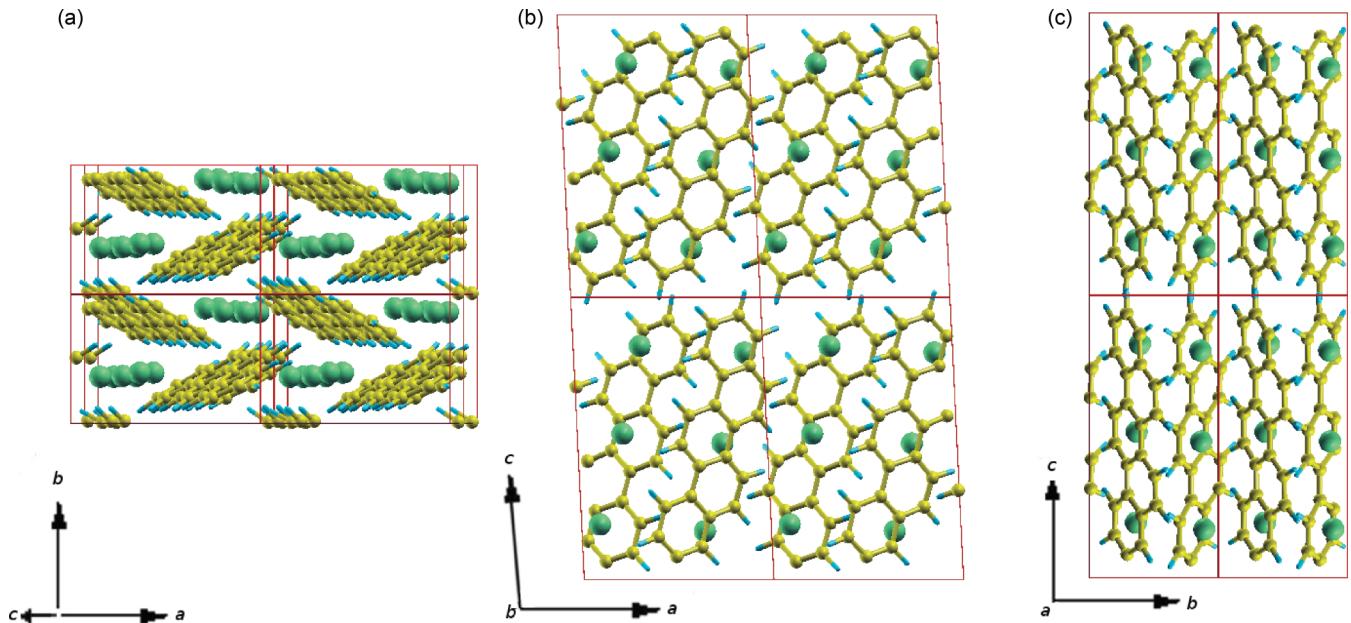


FIG. 1. (Color online) Orthogonal projections of the  $K_3$  picene unit cell, repeated twice along each crystallographic direction. The unit-cell sides are drawn in red. Carbon atoms are in yellow, hydrogen is in blue, and potassium in green. Panel (a):  $ab$  projection with the  $c$  axis pointing outwards. Panel (b):  $ac$  projection with the  $b$  axis pointing inwards. Panel (c):  $bc$  projection with the  $a$  axis pointing inwards.<sup>21</sup>

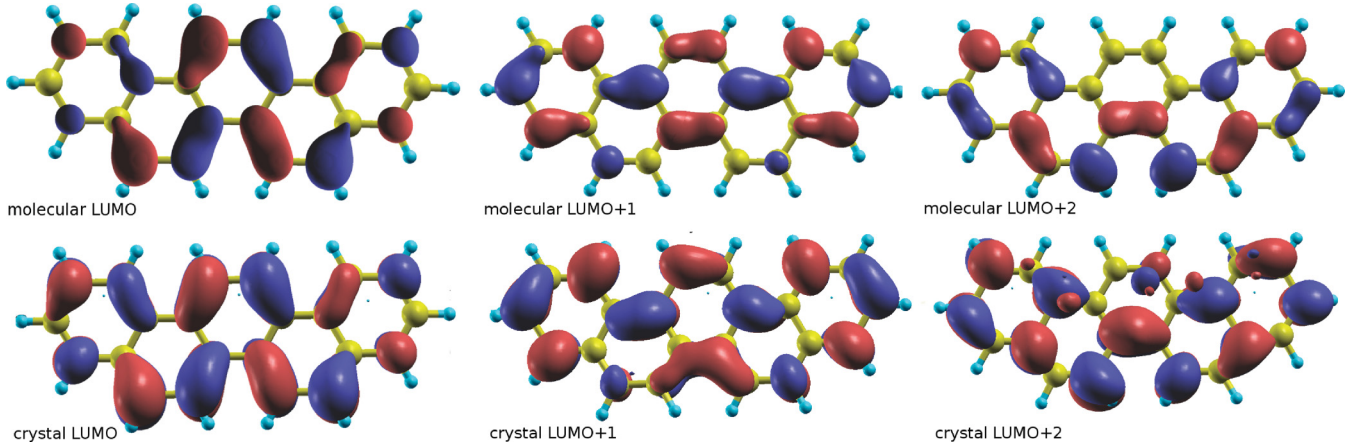


FIG. 2. (Color online) Surface plot of the orbitals of an isolated neutral picene molecule (upper row) and the molecular MLWF functions  $[w_{n0}(\mathbf{r})]$  in the  $K_3$  picene crystal (lower row). The surface is defined by the set of points which satisfies the condition  $|\Psi_n(\mathbf{r})| = 0.05$ , where  $\Psi_n(\mathbf{r}) = \text{Re}[\phi_n(\mathbf{r})]\text{Sign}[\phi_n(\mathbf{r})]$ , with  $\phi_n(\mathbf{r})$  the MO whose phase has been fixed and normalized such that  $\phi_n(\mathbf{r}_{\text{max}}) = 1$ ,  $\mathbf{r}_{\text{max}}$  being the location of the maximum of its modulus (Ref. 21).

where the sum  $\sum_{\mathbf{k}}$  is over a  $N_w$ -point grid in the Brillouin zone (BZ),<sup>23</sup>  $\mathbf{R}$  is a Bravais lattice vector,  $\psi_{m\mathbf{k}}(\mathbf{r})$  are the Bloch eigenstates of the  $m$ th band, and  $\mathbf{U}^{\text{MLWF}}(\mathbf{k})$  is a unitary matrix (for composite bands), defined to minimize the total spread of the wave function

$$\Omega = \sum_n [|\langle \tilde{w}_{n0} | r^2 | \tilde{w}_{n0} \rangle - |\langle \tilde{w}_{n0} | \mathbf{r} | \tilde{w}_{n0} \rangle|^2]. \quad (10)$$

Note that in this case there are two molecules per unit cell, and so the Bravais vectors  $\mathbf{R}$  are not the centers of each molecule, at variance with the simplest case taken into account in Sec. II. In the  $K_3$  picene, the MLWFs have been determined for the bands derived from the lowest unoccupied molecular orbital (LUMO), LUMO + 1, and LUMO + 2 of the neutral picene molecule. Those bands form a quasicomposite group, as the LUMO is well separated from the highest occupied molecular orbital (HOMO). The HOMO-LUMO gap in the pristine picene is 3 eV large,<sup>24</sup> and only the LUMO + 2 is weakly entangled with the upper bands. Therefore, a preliminary disentanglement procedure has been performed<sup>25</sup> before  $\mathbf{U}^{\text{MLWF}}(\mathbf{k})$  could be obtained. Thus, in our case  $\mathbf{U}^{\text{MLWF}}(\mathbf{k})$  is a  $6 \times 6$  matrix (three bands per molecule, two molecules per unit cell), and a tight-binding Hamiltonian can be defined in the rotated MLWF basis, according to the matrix elements

$$H_{nm}(\mathbf{R}) = \langle \tilde{w}_{n0} | H | \tilde{w}_{m\mathbf{R}} \rangle, \quad (11)$$

where  $H$  is the one-body LDA Hamiltonian.

In molecular crystals, the MLWF is not necessarily the best basis to work with. The most “physical” basis is the one which diagonalizes the local part  $[H_{nm}(\mathbf{0})$  and  $(n, m)$  running on the same molecule] of the Hamiltonian in Eq. (11). Indeed, the local part of  $H$  represents the molecule in the crystal, and its eigenvectors  $w_n$  and eigenvalues  $\epsilon_n^{\text{mol}}$  are, respectively, the MOs and molecular levels in the crystal environment. From here on, we define  $w_{n\mathbf{R}}(\mathbf{r})$  to be the “molecular” MLWFs, where  $\mathbf{U}(\mathbf{k}) = \mathbf{U}^{\text{MLWF}}(\mathbf{k}) \times \mathbf{U}_{\text{mol}}$ , with  $\mathbf{U}_{\text{mol}}$  being the unitary transformation which diagonalizes the local problem in the MLWF basis. The molecular MLWFs  $|w_{n\mathbf{R}}\rangle$  obtained in the

rigorous Wannier function formalism play the role of the molecular orbitals  $|i, m\rangle$  generically introduced in Sec. II.

In order to see how the crystal environment affects the local MOs, in Fig. 2 we plotted the local molecular MLWF functions  $w_{n0}(\mathbf{r})$  of  $K_3$  picene together with the MOs of the isolated neutral molecule  $[w_n^{\text{MOL}}(\mathbf{r})]$ . One can see that  $w_{n0}(\mathbf{r})$  in the doped crystal is a good representation of the orbitals in the isolated neutral picene. Indeed, the LUMO and LUMO + 1 are in close agreement. The LUMO + 2 differs only slightly, as in the crystal it is more “delocalized,” something expected as in the molecular calculations its energy level is close to the free particle continuum, and therefore it is more affected by the environment. The overall agreement allows one to make a one-to-one correspondence between the molecular properties and the crystal local on-site properties expressed in the molecular MLWF.

We now analyze the hopping terms in Eq. (11). They show a clear hierarchy in magnitude depending on their spatial direction. The largest are the nearest-neighbor (NN) hoppings which connect the molecules within the herringbone layer. In the herringbone structure, each molecule is linked to its four nearest neighbors in two different ways, by the proximity of either a two-ring molecular side, or a three-ring side [see Fig. 3(a)]. We found that there is a large asymmetry between the NN hoppings connecting two molecules via a three-ring molecular side, dubbed “1D NN” in the text, and the ones whose connection is bridged by a two-ring side, dubbed “2D NN.” The 1D NN terms, sized up to 0.09 eV, are almost twice larger than the 2D NN hoppings, which reach 0.05 eV at most. This is due to the internal degrees of freedom of the single-crystal site, as the picene has an aromatic five-ring structure. If the molecule were symmetric, the 1D and 2D NN hopping terms would be equal. The consequences of this internal asymmetry will be studied later in both the band structure and the electron-phonon couplings.

Not only the NN but also the next-nearest-neighbor (NNN) hoppings are not symmetric. Indeed, the NNN terms pointing along the  $b$  crystallographic axis (named “1D NNN” in the text) are more than twice larger than the ones pointing along

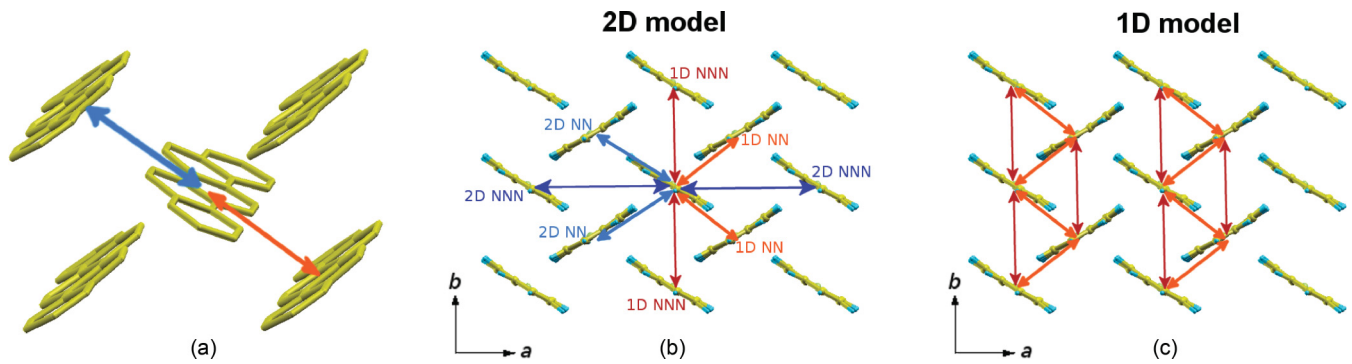


FIG. 3. (Color online) Intermolecular hoppings in the herringbone layer. Panel (a): The two possible nearest-neighbor (NN) intermolecular hoppings are represented, with the strongest in orange (1D NN) mediated by a three-ring molecular side, while the weakest in blue (2D NN) is bridged by a two-ring side. Panel (b): All possible NN and NNN hoppings in the plane are drawn, the 1D NNN are in red and the 2D NN are in dark blue. Panel (c): Two ladder chains formed by selecting only the 1D NN and 1D NNN hoppings, the strongest ones among the bidimensional hoppings.

the  $a$  crystallographic axis (dubbed “2D NNN”), which do not go beyond 0.02 eV. This can be easily explained by noting that the  $b$  axis is shorter than the  $a$  axis, and thus in the  $b$  direction the molecules are more closely packed, with an increase of the transfer integrals and so of the hoppings. See Fig. 3(b) for a graphical representation of all the NN and NNN hoppings in the herringbone plane.

It turns out that the 1D NNN and the 2D NN terms are of the same magnitude ( $\approx 0.05$  eV). The combination of 1D NN and 1D NNN hoppings only, creates ladder chains spanning the  $b$  axis [see Fig. 3(c)], while in a four-hopping model (with the addition of the 2D NN and the 2D NNN terms), their combination spans the full 2D space. The two-ring versus three-ring asymmetry clearly favors a “nematic” one-dimensional electronic structure with respect to the full bidimensional layer. Therefore we define a “1D model” comprised of the 0D (on-site), 1D NN, and 1D NNN terms, and a “2D model” which includes all terms of the “1D model” plus the 2D NN and 2D NNN hoppings.

To understand the impact of this hierarchy on the band structure, we take the hoppings of the tight-binding Hamiltonian written in the MLWF basis, and we are going to selectively switch them on and off. The full band structure is plotted in Fig. 4(d) for the LUMO, LUMO + 1, and LUMO + 2 states, which yield two bands each. By keeping only the local on-site terms, we obtain the molecular levels  $\epsilon_n^{\text{mol}}$  in the crystal, which of course are dispersionless [Fig. 4(a)]. By switching on the 1D NN and the 1D NNN hoppings along the molecular “wire,” one gets the band structure of the 1D model in Fig. 4(b). The dispersion develops only along the  $b$  axis, but it gives the main contribution to the full 3D bandwidth, while the double degeneracy along the CY path is due to the  $P_1^2$  symmetry. The full band structure can be roughly modeled by the 1D model, except that the Fermi surface is poorly reproduced. For the 2D model [see Fig. 1(b)], a band structure closer to the 3D one is obtained, with the LUMO bands almost perfectly reproduced, and the flatness of the BD and CY paths due to the decoupling in the layer stacking.

In the spirit of downfolding the full electronic structure to a low-energy lattice model, one interesting question is whether a two-orbital model is enough to reproduce the low-energy

physics. To this aim, we suppressed the LUMO + 2 orbital from the tight-binding model. The result is shown in Fig. 5. As one can see, the LUMO + 1 bands are strongly deformed, and the Fermi surface is strongly modified. To have a correct description of the low-energy physics of the crystal, one needs also to include the LUMO + 2 molecular orbital. Therefore, a correct modelization of the system comprises three orbitals, up to the LUMO + 2, the hybridization between the LUMO + 1 and LUMO + 2 being very strong.

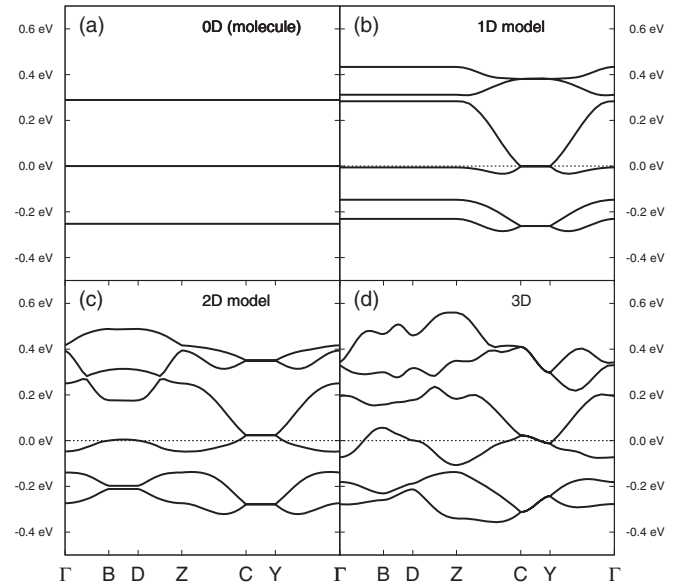


FIG. 4. Band structure of a tight-binding Hamiltonian for the  $K_3$  picene derived in a MLWF basis including LUMO, LUMO + 1, and LUMO + 2 states, plotted along the  $\Gamma$ BZCY $\Gamma$   $k$ -space path. In the reciprocal crystal units, the special points are  $\Gamma = (0,0,0)$ ,  $B = (\frac{1}{2}, 0, 0)$ ,  $D = (\frac{1}{2}, 0, \frac{1}{2})$ ,  $Z = (0, 0, \frac{1}{2})$ ,  $C = (0, \frac{1}{2}, \frac{1}{2})$ , and  $Y = (0, \frac{1}{2}, 0)$ . In the left-upper panel only the “on-site” hoppings have been retained, while in the right-lower panel the band structure has been obtained with the full tight-binding model. The upper-right (the lower-left) panel is the result of a tight-binding model with only 1D (1D + 2D) nearest-neighbor and next-nearest-neighbor hoppings. The zero of the energy axis is the Fermi level.

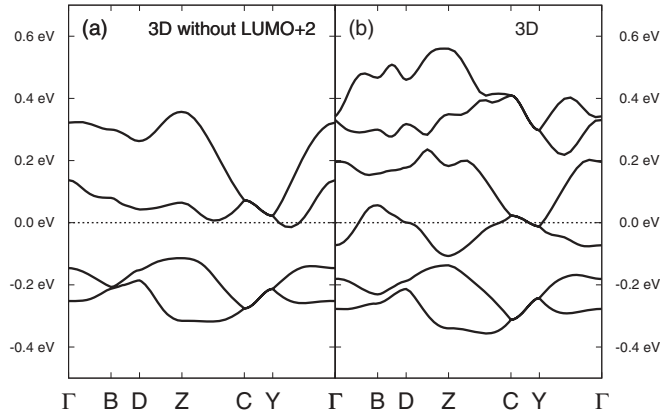


FIG. 5. The full band structure (right) and the one obtained by taking off the LUMO + 2 states (left) from the tight-binding Hamiltonian obtained in the molecular MLWF basis for the  $K_3$  picene. The definition of the high-symmetry points in the  $k$  path is reported in the caption of Fig. 4. The zero of the energy axis is the Fermi level.

#### A. Technical details for the band structure calculations

The LDA-DFT calculations have been performed with the QUANTUM-ESPRESSO<sup>26</sup> code. K, C, and H atoms are described by ultrasoft pseudopotentials. The plane-wave (PW) cutoff is 60 Ry for the wave function and 600 Ry for the charge. A  $4 \times 4 \times 4$  electron-momentum grid and a Methfessel-Paxton smearing of 0.015 Ry are used in the electronic integration.

Wannierization has been performed with the WANNIER90<sup>27</sup> program on a  $N_w = 4 \times 4 \times 4$  electron-momentum mesh by including the LUMO, LUMO + 1, and LUMO + 2 states. Both the long-range hoppings and inclusion of the first three LUMOs are needed to get localized orbitals and Wannierized bands in a very good agreement with those computed in the PW basis set in a window of  $\pm 0.3$  eV around the Fermi level. Indeed, the maximum discrepancy between the *ab initio* bands and the Wannierized ones is only 5 meV for the LUMO and LUMO + 1 states, while it is larger (0.05 eV at most) for the LUMO + 2 band, which is, however, higher in energy.

The spreads  $\Omega_n = \langle \tilde{w}_{n0} | r^2 | \tilde{w}_{n0} \rangle - |\langle \tilde{w}_{n0} | r | \tilde{w}_{n0} \rangle|^2$  of the  $n$ th MLWF  $\tilde{w}_{nR}(\mathbf{r})$  are 11.8 Å, 13.2 Å, and 21.1 Å for  $n = 1, 2$ , and 3, respectively. The  $n = 3$  MLWF orbital is more spread out and leads to a LUMO + 2 molecular orbital more sensitive to the crystal environment, as highlighted by Fig. 2.

#### IV. LOCAL AND NONLOCAL ELECTRON-PHONON COUPLINGS IN $K_3$ PICENE

The total electron-phonon coupling is  $\lambda = \frac{1}{N_q} \sum_{\mathbf{q}\nu} \lambda_{\mathbf{q}\nu}$ , where  $\nu$  is the phonon mode and  $\mathbf{q}$  is its momentum. The phonon-resolved coupling reads

$$\lambda_{\mathbf{q}\nu} = \frac{2}{\omega_{\mathbf{q}\nu}^2 N(0)} \frac{1}{N_{\mathbf{k}}} \sum_{\mathbf{k}} \sum_{n,m} |g_{\mathbf{k}n,\mathbf{k}+\mathbf{q}m}^{\nu}|^2 \times (f_{\mathbf{k}n} - f_{\mathbf{k}+\mathbf{q},m}) \delta(\epsilon_{\mathbf{k}+\mathbf{q},m} - \epsilon_{\mathbf{k}n} - \omega_{\mathbf{q}\nu}), \quad (12)$$

which couples the occupied state  $|\mathbf{k}, n\rangle$  (the ket refers to the periodic part of the Bloch function) of momentum  $\mathbf{k}$  and band  $n$  with the empty state  $|\mathbf{k} + \mathbf{q}, m\rangle$  separated by the phonon energy

$\omega_{\mathbf{q}\nu}$ .  $N(0)$  is the electron DOS per spin per cell at the Fermi level. The electron-phonon matrix elements are  $g_{\mathbf{k}n,\mathbf{k}+\mathbf{q}m}^{\nu} = \sum_s \mathbf{e}_{\mathbf{q}\nu}^s \cdot \mathbf{d}_{mn}^s(\mathbf{k} + \mathbf{q}, \mathbf{k}) / \sqrt{2M_s \omega_{\mathbf{q}\nu}}$ , where  $\mathbf{d}_{mn}^s(\mathbf{k} + \mathbf{q}, \mathbf{k}) = \langle \mathbf{k} + \mathbf{q}, m | \delta v_{\text{SCF}} / \delta u_{\mathbf{q}s} | \mathbf{k}, n \rangle$ , with  $\delta v_{\text{SCF}} / \delta u_{\mathbf{q}s}$  the periodic part of the DFT screened deformation potential. In Eq. (12),  $f_{\mathbf{k}n}$  are Fermi functions depending on the temperature  $T$ , and the expression for  $\lambda_{\mathbf{q}\nu}$  has to be evaluated by a  $T \rightarrow 0$  extrapolation. In the ‘‘adiabatic’’ limit, namely, for  $\omega_{ph} \ll \Delta\epsilon$ , where  $\Delta\epsilon$  is the bandwidth and  $\omega_{ph}$  is the characteristic phonon frequency, the expression for  $\lambda_{\mathbf{q}\nu}$  in Eq. (12) reduces to the one proposed by Allen,<sup>28</sup> generally used in previous electron-phonon estimates:

$$\lambda_{\mathbf{q}\nu}^{\text{AD}} = \frac{2}{\omega_{\mathbf{q}\nu} N(0)} \frac{1}{N_{\mathbf{k}}} \sum_{\mathbf{k}} \sum_{n,m} |g_{\mathbf{k}n,\mathbf{k}+\mathbf{q}m}^{\nu}|^2 \delta(\epsilon_{\mathbf{k},n}) \delta(\epsilon_{\mathbf{k}+\mathbf{q},m}). \quad (13)$$

We are going to dub  $\lambda^{\text{AD}}$  in the equation above as ‘‘adiabatic,’’ while  $\lambda$  in Eq. (12) we dub ‘‘nonadiabatic.’’

By exploiting the definition of Wannier functions in Eq. (9), the deformation potential matrix elements  $\mathbf{d}_{mn}^s(\mathbf{k} + \mathbf{q}, \mathbf{k})$  can be written in terms of the molecular MWLF basis as

$$\mathbf{d}_{mn}^s(\mathbf{k} + \mathbf{q}, \mathbf{k}) = \sum_{\mathbf{R}} \sum_{m'n'} e^{i\mathbf{k}\cdot\mathbf{R}} U_{mm'}(\mathbf{k} + \mathbf{q}) \mathbf{d}_{m'n'}^{\text{qs}}(\mathbf{R}) U_{nn'}^*(\mathbf{k}), \quad (14)$$

where the deformation potential in the MLWF local representation is

$$\mathbf{d}_{mn}^{\text{qs}}(\mathbf{R}) = \langle w_{m0} | \frac{\delta v_{\text{SCF}}}{\delta u_{\mathbf{q}s}} | w_{nR} \rangle. \quad (15)$$

Equation (15) is analogous to Eq. (11) but for the electron-phonon coupling elements, when only the localization of the wave function is used. Therefore, the same analysis carried out in Sec. III can be done here, with the distinction between the ‘‘local’’ [with  $\mathbf{R} = \mathbf{0}$  and  $(m,n)$  orbitals on a single molecule] and ‘‘nonlocal’’ [with  $\mathbf{R} \neq \mathbf{0}$ , or  $\mathbf{R} = \mathbf{0}$  with  $(m,n)$  orbitals centered on two different molecules of the unit cell] matrix elements. Thus, it is the Wannier function formalism which allows one to make the bridge from the plane-wave representation to the molecular-orbital description of the electron-phonon problem introduced in Sec. II, with the distinction between local and nonlocal couplings.

As already pointed out in Sec. II, an analogous but independent definition of local and nonlocal contributions can be done not only for the electronic states, but also for the phonon modes. To project the phonon vibrations we use the same strategy as reported in Ref. 16, namely, we introduce a  $3N \times 3N$  tensor  $\mathcal{P}_S$ , which projects on either the intramolecular modes or the ensemble of K and intermolecular modes.  $\mathcal{P}_S$  acts on the 3D eigenphonons  $\mathbf{e}_{\mathbf{q}\nu}$ , such that one can define the phonon-projected matrix elements as  $g_S = \sum_s (\mathcal{P}_S \mathbf{e}_{\mathbf{q}\nu})^s \cdot \mathbf{d}_{nm}^s(\mathbf{k}, \mathbf{k} + \mathbf{q}) / \sqrt{2M_s \omega_{\mathbf{q}\nu}}$ . The resulting phonon-projected  $\lambda$  is then

$$\lambda_{\mathbf{q}\nu}^{S,S'} = \frac{2}{\omega_{\mathbf{q}\nu}^2 N(0)} \frac{1}{N_{\mathbf{k}}} \sum_{\mathbf{k}, n, m} g_S g_{S'}^* \times (f_{\mathbf{k}n} - f_{\mathbf{k}+\mathbf{q},m}) \delta(\epsilon_{\mathbf{k}+\mathbf{q},m} - \epsilon_{\mathbf{k}n} - \omega_{\mathbf{q}\nu}). \quad (16)$$

TABLE I. Adiabatic  $\lambda^{\text{AD}}$  and nonadiabatic  $\lambda$  computed via Eqs. (13) and (12), respectively, for selected electron-phonon couplings, corresponding to Fig. 6. We report also the phonon frequency logarithmic average  $\omega_{\log}$  for both the adiabatic and nonadiabatic formulations. “Full el-phon” means that all terms are taken from the *ab initio* calculation of the electron-phonon coupling, “local el-phon” means that only local terms are retained in  $\mathbf{d}_{m'n'}^{\text{qs}}(\mathbf{R})$ , while “nonlocal el-phon” refers to the case where only off-site terms are taken in  $\mathbf{d}_{m'n'}^{\text{qs}}(\mathbf{R})$ . In the “local el-phon with intraphonons,” not only the deformation potential but also the phonon eigenmodes are projected on the molecule.

Model	$\lambda^{\text{AD}}$	$\lambda$	$\omega_{\log}^{\text{AD}}$ (meV)	$\omega_{\log}$ (meV)
Full el-phon	0.88	0.73	25	18
Nonlocal el-phon	0.65	0.60	17	14
Local el-phon	0.25	0.17	63	41
Local el-phon with intraphonons	0.20	0.12	93	68

The total  $\lambda$  is  $\sum_{S,S'} \lambda^{S,S'} = \sum_{S,S'} \frac{1}{N_q} \sum_{\mathbf{q}_v} \lambda_{\mathbf{q}_v}^{S,S'}$ . The contribution of each subspace S is computed as  $\sum_{S'} \lambda^{S,S'}$ , where we add both the diagonal term and the usually very small off-diagonal contributions. The results of this analysis are reported in Table I and Fig. 6.

In Fig. 6 we plot the Eliashberg function  $\alpha^2 F(\omega) = \sum_{\mathbf{q}_v} \lambda_{\mathbf{q}_v} \omega_{\mathbf{q}_v} \delta(\omega - \omega_{\mathbf{q}_v}) / (2N_q)$  and the integral  $\lambda(\omega) = 2 \int_0^\omega d\omega' \alpha^2 F(\omega') / \omega'$ , namely, the frequency-resolved electron-phonon coupling. The first row is the total  $\lambda$  computed by means of Eqs. (13) and (12) by including all (local and nonlocal) electron-phonon contributions. This result has been already reported in Ref. 16. In the second row, we plot  $\lambda$  where only nonlocal matrix elements are taken. This accounts for 72% (80%) of the total  $\lambda$  in the adiabatic (nonadiabatic) formulation. In this case, the main contribution to the electron-phonon coupling comes from intermolecular soft phonon modes, with strong spectral weight at low frequencies ( $< 500 \text{ cm}^{-1}$ ). In the third row of Fig. 6, we plot the coupling arising only from local matrix elements. The corresponding  $\alpha^2 F(\omega)$  is peaked around frequencies related to in-plane molecular phonon modes, which give the main contribution to the local electron-phonon coupling. In the lower row, not only the deformation potential matrix elements but also the phonon modes are projected on each molecule. The band structure ( $\epsilon_{k_n}$ ) and the phonon spectrum ( $\omega_{\mathbf{q}_v}$ ) are instead unmodified with respect to the full solid. Therefore the latter case is the closest estimate of the electron-phonon coupling of a single (doped) molecule placed in the crystal metallic environment. The projection of the phonon eigenmodes on the molecular subspace further reduces  $\lambda$ . We reach therefore one of the main conclusions of this work. The purely molecular contributions (filtered in both the wave function and eigenphonons) are such that the resulting  $\lambda$  accounts for only 23% (17%) of the full  $\lambda$  in the adiabatic (nonadiabatic) formulation. All the rest comes from nonlocal sources. Note also in Table I that the phonon frequency logarithmic average  $\omega_{\log}$  varies substantially with respect to the model. The nonlocal contributions drastically reduce the  $\omega_{\log}$  value, which corresponds to a lower estimate of  $T_c$ , which depends linearly on  $\omega_{\log}$ , according to McMillan.<sup>29</sup>

### A. Technical details for the electron-phonon calculations

In order to evaluate the electron-phonon coupling in the  $\text{K}_3$  picene, we first carried out phonon calculations in the density-functional perturbation theory framework (DFPT)<sup>30</sup> on a  $N_q = 2 \times 2 \times 2$  grid of phonon momenta  $\mathbf{q}$ , as illustrated in Ref. 16. The electronic grid used in DFPT has a mesh of  $2 \times 2 \times 2$  points with a Methfessel-Paxton smearing of 0.03 Ry. For each phonon mode  $\nu$  with momentum  $\mathbf{q}$  we computed both the “nonadiabatic” electron-phonon interaction in Eq. (12) and the “adiabatic” one in Eq. (13). The  $\mathbf{k}$  summation in both equations has been performed by means of the Wannier interpolation technique<sup>27,31–33</sup> in the MLWF basis. The convergence in the  $\mathbf{k}$  summation was reached for a  $N_k = 60 \times 60 \times 60$  momentum grid, with temperature and smearing given by  $T = 150 \text{ K}$  and  $\sigma = 4.3 \text{ meV}$ , respectively, with  $T = 3\sigma$ .

The matrix elements  $g_{k_n, \mathbf{k}+\mathbf{q}_m}^{\nu}$  have been computed by selecting the local and nonlocal contributions in the deformation potential [through the MLWF via Eq. (15)] and the phonon modes (through the phonon projector  $\mathcal{P}_S$ ).

With the smearing and  $\mathbf{k}$ -point grid at convergence, we checked the accuracy of the extrapolated value of the Fermi level  $\epsilon_F$  by comparing it to the value obtained by an *ab initio* calculation with a large  $\mathbf{k}$ -grid ( $N_k = 10 \times 10 \times 10$ ) and a small Gaussian smearing (0.002 Ry). The uncertainty in  $\epsilon_F$  is of the order of 1 meV, giving rise to a change in the density of state  $N(0)$  of only 1%. Thus, a comparable error occurs in  $\lambda$  from the  $\epsilon_F$  position.

Thanks to the Wannier interpolation, the electronic  $\mathbf{k}$  summation in the electron-phonon coupling  $\lambda_{\mathbf{q}}$  is converged for each  $\mathbf{q}$ . The main residual error in the total  $\lambda$  comes from the coarse  $N_q = 2 \times 2 \times 2$  momentum grid used in the  $\mathbf{q}$  summation of  $\lambda_{\mathbf{q}}$ . An estimate of this error was done in Ref. 16 by studying the fluctuations of  $\lambda_{\mathbf{q}}$  over the  $\mathbf{q}$ -point sampling. We found that the uncertainty on  $\lambda$  goes from about 20% for the adiabatic values to less than 15% for the nonadiabatic estimates, while the error on the relative contributions (i.e., ratio of local  $\lambda$  over nonlocal  $\lambda$ ) is even smaller (less than 10%).

## V. SCREENING OF LOCAL ELECTRON-PHONON COUPLINGS

The result presented in the previous section is completely unexpected if one follows the common wisdom that molecular crystals can be reliably described by molecular derived quantities.<sup>34,35</sup> For instance, molecular electron-phonon calculations have been used to compute  $\lambda$  in molecular crystals.<sup>36,37</sup> This has been the case of some previously published works on the doped  $\text{C}_{60}$  (Refs. 12,13,38–40) and the newly discovered “aromatic” superconductors.<sup>14,36,37,41,42</sup> Here, we show that at least in the  $\text{K}_3$  picene, molecular-only calculations are not reliable to predict the crystal total  $\lambda$ . Presumably, this applies also to the whole series of new aromatic superconductors, where the physics should be similar.<sup>9</sup>

To explain why the intramolecular electron-phonon coupling is so weak in the crystal, we carried out electronic-structure and phonon calculations for the isolated neutral molecule in the same QUANTUM-ESPRESSO<sup>26</sup> PW framework. The resulting electron-phonon coupling values are

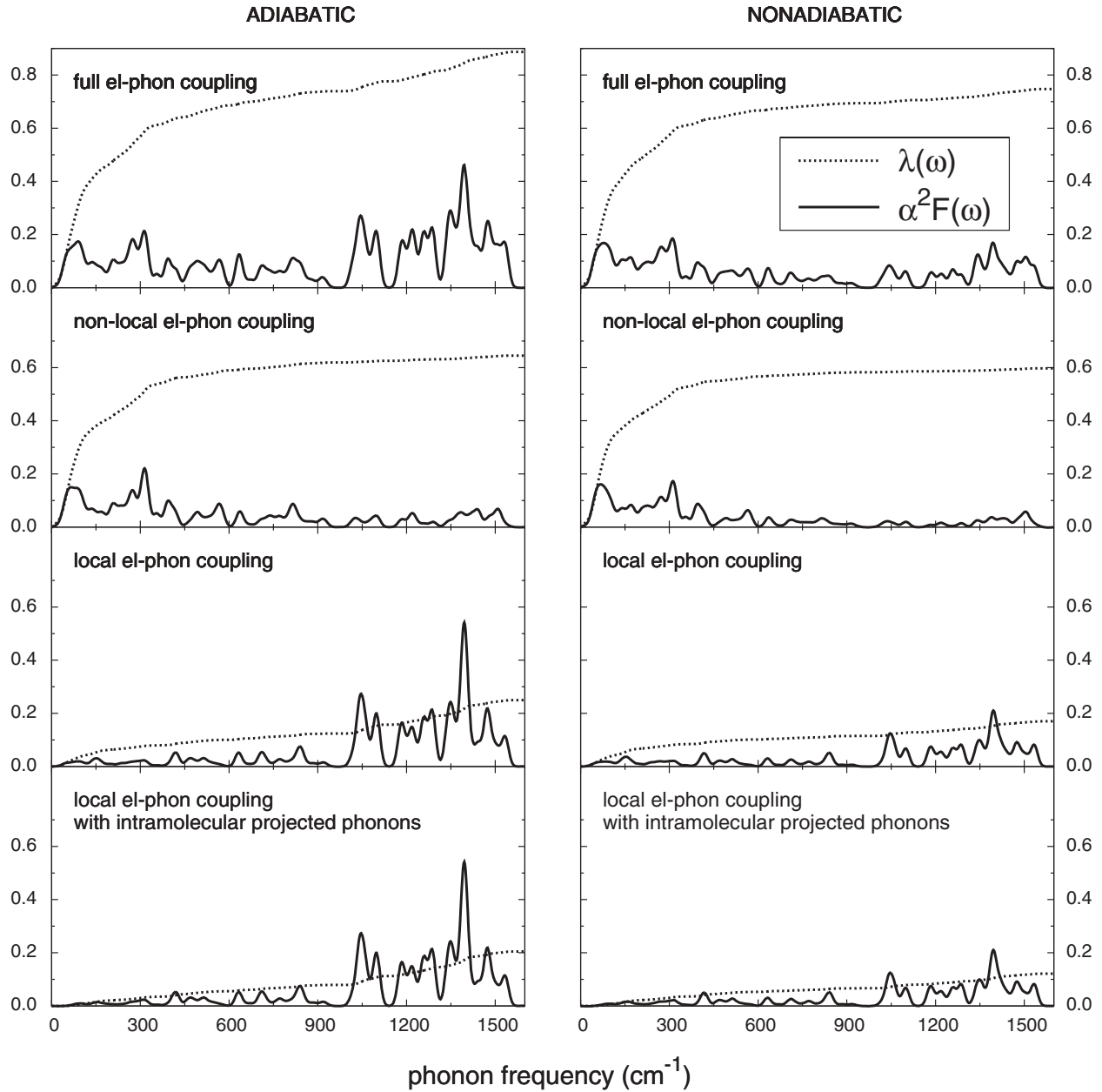


FIG. 6. Eliashberg  $\alpha^2 F$  and integrated  $\lambda$  for various electron-phonon coupling models. All *ab initio* elements are taken in the first row, the second row is for the nonlocal  $\mathbf{d}_{m'n'}^{\text{qs}}(\mathbf{R})$  terms, and the third and fourth rows are for the on-site coupling. In the latter also the phonon eigenmodes are projected on the intramolecular subspace. To the left we show quantities computed by the adiabatic approximation [Eq. (13)], and to the right those evaluated by Eq. (12).

in good agreement with previous molecular calculations by Kato *et al.*<sup>14</sup>

The isolated molecule calculations allowed us to compute also the *molecular* deformation potential in the MO representation:

$$\mathbf{d}_{mn}^{\text{sMOL}} = \langle w_m^{\text{MOL}} | \frac{\delta V_{\text{SCF}}^{\text{MOL}}}{\delta \mathbf{u}_s} | w_n^{\text{MOL}} \rangle, \quad (17)$$

where now  $\mathbf{d}_{mn}^{\text{sMOL}}$  is  $\mathbf{q}$  independent. By replacing  $\mathbf{d}_{mn}^{\text{qs}}(\mathbf{0})$  with  $\mathbf{d}_{mn}^{\text{sMOL}}$  in Eq. (14), and by taking only the local contributions [namely,  $\mathbf{R} = \mathbf{0}$  and  $(m, n)$  running on the same molecule], one can directly compare the difference between  $\frac{\delta V_{\text{SCF}}^{\text{MOL}}}{\delta \mathbf{u}_s}$  and  $\frac{\delta v_{\text{SCF}}}{\delta \mathbf{u}_{\text{qs}}}$  on the resulting  $\lambda$ . Indeed, we have already shown that the MOs

$w_m^{\text{MOL}}$  are very close to the molecular MLWF  $w_{m\mathbf{R}}$  (see Fig. 2), so that a difference in  $\lambda$  can come only from the deformation potential operator. Moreover, we noticed that the  $\mathbf{q}$  dependence of  $\mathbf{d}_{mn}^{\text{qs}}(\mathbf{0})$  is very weak, and so a direct comparison can be made at each crystal phonon momentum  $\mathbf{q}$ . The molecular  $\frac{\delta V_{\text{SCF}}^{\text{MOL}}}{\delta \mathbf{u}_s}$  is the “bare” one, while  $\frac{\delta v_{\text{SCF}}}{\delta \mathbf{u}_{\text{qs}}}$  is screened by the crystal environment and by the partially occupied metallic bands of LUMO + 1 character.

From here on, our estimates of  $\lambda$  are based only on the adiabatic approximation in Eq. (13). Although we have seen that it is less accurate than the nonadiabatic formula, we are going to use it because from the adiabatic formulation it is easier to make the connection to the molecular approximation

TABLE II.  $\lambda^{\text{AD}}$  corresponding to the integrated  $\alpha^2 F$  functions plotted in Fig. 7. Row order corresponds to the label sequence of the figure. The phonon frequency logarithmic average  $\omega_{\log}^{\text{AD}}$  is also reported.

Model	$\lambda^{\text{AD}}$	$\omega_{\log}^{\text{AD}}$ (meV)
Crystal local el-phon with crystal intraphonons	0.20	93
Molecular el-phon with crystal intraphonons	0.78	96
Crystal local el-phon with molecular phonons	0.15	110
Molecular el-phon with molecular phonons	0.57	125

formula<sup>43</sup> for  $\lambda$  and make the comparison with previous works (which mainly used the adiabatic approximation). The results are plotted in Fig. 7 and reported in Table II. By comparing panels (a) and (b), it turns out that the total coupling  $\lambda$  with the screened deformation potential is about 4 times weaker, which implies that on average the electron-phonon matrix elements  $g_{\mathbf{kn},\mathbf{k}+\mathbf{qm}}^{\nu}$  are twice smaller than the “bare” ones of the isolated neutral molecule.

Therefore, we reach our second main conclusion of this work. Describing correctly the effect of the metallic screening provided by the crystal environment to the deformation potential is critical to get the right estimate of the electron-phonon coupling.

Now, let us analyze in detail the effect of the metallic crystal environment on the dynamical matrix, and so on the phonons. In Eq. (13), we replace the phonon eigenvalues

$\omega_{\mathbf{qv}}$  and eigenvectors  $\mathbf{e}_{\mathbf{qv}}$  with the corresponding molecular  $\omega_{\nu}^{\text{MOL}}$  and  $\mathbf{e}_{\nu}^{\text{MOL}}$ , computed for the isolated undoped picene molecule. The results are reported in Figs. 7(c) and 7(d). If compared to panels (a) and (b), there is a global frequency softening of  $50 \text{ cm}^{-1}$  for the in-plane phonons in the crystal induced by the doping. The second effect is a remodulation of the frequency dependence of the electron-phonon coupling strength. In the  $\alpha^2 F(\omega)$  obtained with molecular phonons, the coupling is mostly peaked around  $1600 \text{ cm}^{-1}$ , while it is much more broadly distributed in the crystal phonons.

From this analysis we can conclude that upon doping the metallic environment provided by the crystal strongly affects both the deformation potential and the dynamical matrix. The metallic screening reduces the electron-phonon coupling strength, while it softens the phonon modes and makes their coupling to the charge broader in the phonon frequency.

The  $\alpha^2 F(\omega)$  plotted in Fig. 7(d) for molecular phonons and molecular  $\frac{\delta V_{\text{SCF}}^{\text{MOL}}}{\delta \mathbf{u}_{\nu,0}}$  closely resembles the one published in Ref. 15, where the deformation potential and the dynamical matrix have been computed for the undoped insulating picene crystal in the rigid doping approximation. Thus, the effect of the metallic screening from partially filled bands has been neglected in both the deformation potential and the dynamical matrix. The value of  $\omega_{\log}^{\text{AD}}$  corresponding to the Eliashberg function of Fig. 7(d) is 125 meV, very close to the value reported in Ref. 15 (126 meV). This is a further indication that erroneous results can be obtained for doped picene if the metallic screening is not included in the calculations.

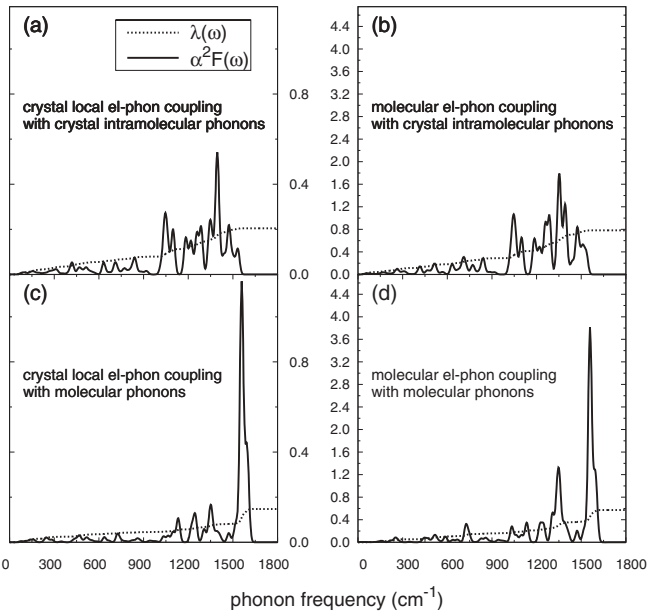


FIG. 7. Eliashberg function  $\alpha^2 F$  and the adiabatic  $\lambda^{\text{AD}}$  computed via Eq. (13) for both crystal local  $\mathbf{d}$  [panels (a) and (c)] and purely molecular  $\mathbf{d}^{\text{MOL}}$  [panels (b) and (d)]. In the formula, we used either the intramolecular projected phonons  $\mathbf{e}_{\mathbf{qv}}$  [panels (a) and (b)] or the purely molecular dynamical matrix [panels (c) and (d)]. Note that the y-axis scale of the left panels is 4 times wider than the scale on the right panels to show that the magnitude of the local  $\mathbf{d}$  (averaged over the phonon momenta  $\mathbf{q}$  and the phonon modes  $\nu$ ) is about 4 times smaller than the magnitude of  $\mathbf{d}^{\text{MOL}}$  (averaged over the molecular phonon modes  $\nu$ ).

#### A. Technical details for the molecular electron-phonon calculations

The molecular DFT calculations have been carried out with the PW basis set in the same supercell as the one of the  $K_3$  picene, where only one of the two molecules per crystal unit cell has been taken. We checked that the  $K_3$  picene supercell is large enough to get the same molecular levels as the ones of a much larger supercell, and thus the boundary effects are negligible. We left the atomic positions of the molecule unchanged from the crystal, in such a way that the deformation potential calculated for the molecule could directly replace the one for the crystal in  $g_{\mathbf{kn},\mathbf{k}+\mathbf{qm}}^{\nu}$  of Eqs. (12) and (13) without any particular rotation in the coordinate space. The DFT calculation of the molecule was performed in its neutral state, at the  $\Gamma$  point. The electron-phonon calculations were performed at  $\mathbf{q} = (\frac{1}{2}, \frac{1}{2}, \frac{1}{2})$  (in crystal fractional coordinates) to avoid the effective charge contributions to the deformation potential, which results in the Fröhlich Hamiltonian<sup>44</sup> and diverges for zone-center optical phonons.

### VI. IMPACT OF DIMENSIONALITY ON NONLOCAL ELECTRON-PHONON COUPLINGS

In this section we want to go beyond the distinction between intramolecular local and intermolecular nonlocal couplings, and analyze what are the most important electron-phonon interactions among the nonlocal contributions. We keep a “direct space” approach in labeling the various terms by exploiting the local picture provided by the molecular MLWFs. In other words, we aim at finding the minimal electron-phonon

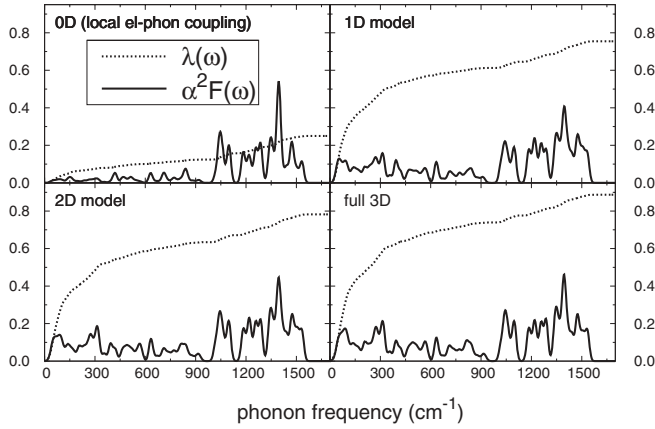


FIG. 8. Eliashberg function  $\alpha^2 F$  computed with the adiabatic formulation [Eq. (13)] for various electron-phonon coupling models, based on a selection of the deformation potential  $\mathbf{d}(\mathbf{R})$  terms. The 1D model gives 85% of the total  $\lambda$  by keeping almost all of the dominant low-frequency contributions related to the coupling with the intermolecular phonons.

lattice model (where each lattice site represents the center of a picene molecule), which gives the closest possible description to the full “*ab initio*” Hamiltonian.

In practice, we select a subset of possible elements in the deformation potential matrix expressed in the molecular MLWF basis [Eq. (15)]. According to the set of Bravais vectors  $\mathbf{R}$  and Wannier function indices  $(m, n)$ , it is possible to restrict the coupling to be local (0D), unidimensional (1D) with molecular chains oriented along the  $b$  crystallographic axis, bidimensional (2D) with molecular layers spanning planes containing the  $a$  and  $b$  crystallographic axes, or the full “*ab initio*” model without constraints. It is also possible to select the neighboring molecules based on their distance, therefore distinguishing between nearest neighbors (NN) and next-nearest neighbors (NNN) on a given direction. In Sec. III, we introduced the 1D and 2D models for the hoppings. The same models apply also for the deformation potential matrix elements.

The results are reported in Fig. 8 and Table III. The 1D model gives 85% of the total  $\lambda$ . The 2D model, where also the 2D NN and 2D NNN contributions are added, yields 90% of the total electron-phonon coupling. From the  $\alpha^2 F(\omega)$  in the upper-rightmost panel of Fig. 8, it is apparent that in the 1D model the strongest coupling originates from out-of-plane

TABLE III.  $\lambda$  computed via Eq. (13) for various electron-phonon coupling models, corresponding to Fig. 8.  $\omega_{\log}^{\text{AD}}$  is the phonon frequency logarithmic average. “0D” means that only local molecular couplings are retained in the deformation potential matrix elements, “1D” refers to the one-dimensional model of chains along the  $b$  crystallographic axis, and “2D” is the model for the molecular herringbone layer spanning the  $a$  and  $b$  axes.

Model	$\lambda^{\text{AD}}$	$\omega_{\log}^{\text{AD}}$ (meV)
0D	0.25	63
1D	0.74	26
2D	0.77	27
Full 3D	0.88	25

vibrations and intermolecular phonons, as a large contribution comes from frequencies below  $300 \text{ cm}^{-1}$ .

This is the third important result of this work. One can model the system by *few* non-local electron-phonon couplings [Eq. (7)] added to the local Holstein-like terms [Eq. (6)]. As the local terms are weak (see Sec. V), those few nonlocal couplings are responsible for more than 60% of the total  $\lambda$ . This opens the way toward an efficient and reliable lattice modelization of the system, where more sophisticated many-body techniques can be used to deal with the electronic correlation and electron-phonon coupling together.

It is striking that the main contribution to the coupling (more than 50%) comes from the phonon-modulated hoppings in the  $b$  crystallographic direction, meaning that the electron-phonon coupling is strongly anisotropic along molecular chains. Based on the molecular arrangement of the crystal and on the band structure, one would have instead expected a planar anisotropy, as the system is layered, with planes oriented in the  $a$ - $b$  directions. On the contrary, there is no clear distinction in magnitude between the in-plane and the out-of-plane matrix elements, except for the hierarchy between the strong 1D components and the rest. From this point of view, the material behaves more like an array of chains rather than an array of planes. The 1D anisotropy is a consequence of the asymmetry of the picene armchair structure, as already shown in Sec. III.

In order to generalize this argument to the experimental situations and other superconducting aromatic crystals, caution must be taken in view of the importance of the arrangement of the molecules, and of disorder. Even though the connection between molecular shape and electron-phonon anisotropy is intrinsic and thus disorder-independent, disorder in experiments can affect the local geometry and change the total electron-phonon coupling strength.

## VII. CONCLUSIONS

In this paper we went beyond what we have done in Ref. 16, where we carried out a detailed analysis of the electron-phonon coupling based on the phonon projection to intramolecular and intermolecular eigenmodes. Here, thanks to the maximally localized Wannier function formalism, we took into account also the electronic projection of the deformation potential into local (Holstein-like) and nonlocal couplings, defined based on a molecular-orbital representation. We found that the purely molecular contribution (projected in both the deformation potential and phonon eigenmodes) is very weak. It accounts for only 20% of the total  $\lambda$  [in the adiabatic coupling formulation of Eq. (13)]. It is therefore impossible to predict the total coupling of  $\text{K}_3$  picene with isolated molecular calculations only. We understood this as an effect of the metallic screening, which mainly reduces the deformation potential matrix elements. This turns out from a direct comparison of the projected local coupling in the crystal with the full coupling in the isolated molecule, carried out within the same theoretical framework.

Moreover, we demonstrated that while 80% of the electron-phonon coupling in  $\text{K}_3$  picene is nonlocal, more than 60% of  $\lambda$  comes just from *two* terms, i.e., the 1D nearest neighbor (NN) and the 1D next-nearest-neighbor (NNN)

phonon-modulated hoppings, which form ladder chains along the  $b$  crystallographic axis of the compound.

The strong spatial 1D anisotropy of the electron-phonon coupling is another interesting outcome of the present work. The intermolecular modes couple more strongly with the electrons along chains of molecules, arranged in an ordered array of ladders. We related this to the picene molecular edge asymmetry in its armchair structure.

Finally, we showed that the model comprised of local, 1D NN, and 1D NNN contributions yields 85% of the total electron-phonon coupling of the crystal. This *ab initio* modelization opens the way to reliable and quantitative

many-body calculations on the lattice, in order to study the interplay between strong electronic correlation (typical of a molecular crystal with flat bands<sup>45–47</sup>) and electron-phonon coupling in  $K_3$  picene.

## ACKNOWLEDGMENTS

We acknowledge M. Fabrizio, T. Kato, Y. Kubozono, G. Profeta, and S. Taioli for useful discussions. M. Casula thanks GENCI for the HPC resources obtained under Grant No. 2012096493.

- 
- <sup>1</sup>V. C. Sundar, J. Zaumseil, V. Podzorov, E. Menard, R. L. Willett, T. Someya, M. E. Gershenson, and J. A. Rogers, *Science* **303**, 1644 (2004).
- <sup>2</sup>J. Takeya, M. Yamagishi, M. Tominari, R. Hirahara, Y. Nakazawa, T. Nishikawa, T. Kawase, T. Shimoda, and S. Ogawa, *Appl. Phys. Lett.* **90**, 102120 (2007).
- <sup>3</sup>H. Okamoto, N. Kawasaki, Y. Kaji, Y. Kubozono, A. Fujiwara, and M. Yamaji, *J. Am. Chem. Soc.* **130**, 10470 (2008).
- <sup>4</sup>N. Kawai, R. Eguchi, H. Goto, K. Akaike, Y. Kaji, T. Kambe, A. Fujiwara, and Y. Kubozono, *J. Phys. Chem. C* **116**, 7983 (2012).
- <sup>5</sup>M. F. Craciun, S. Rogge, M. J. L. den Boer, S. Margadonna, K. Prassides, Y. Iwasa, and A. G. Morpurgo, *Adv. Mater.* **18**, 320 (2006).
- <sup>6</sup>R. Mitsuhashi, Y. Suzuki, Y. Yamanari, H. Mitamura, T. Kambe, N. Ikeda, H. Okamoto, A. Fujiwara, M. Yamaji, N. Kawasaki, Y. Maniwa, and Y. Kubozono, *Nature (London)* **464**, 76 (2010).
- <sup>7</sup>X. F. Wang, R. H. Liu, Z. Gui, Y. L. Xie, Y. J. Yan, J. J. Ying, X. G. Luo, and X. H. Chen, *Nat. Commun.* **2**, 507 (2011).
- <sup>8</sup>X. F. Wang, Y. J. Yan, Z. Gui, R. H. Liu, J. J. Ying, X. G. Luo, and X. H. Chen, *Phys. Rev. B* **84**, 214523 (2011).
- <sup>9</sup>Y. Kubozono, H. Mitamura, X. Lee, X. He, Y. Yamanari, Y. Takahashi, Y. Suzuki, Y. Kaji, R. Eguchi, K. Akaike, T. Kambe, H. Okamoto, A. Fujiwara, T. Kato, T. Kosugi, and H. Aoki, *PhysChemChemPhys* **13**, 16476 (2011).
- <sup>10</sup>M. Xue, T. Cao, D. Wang, Y. Wu, H. Yang, X. Dong, J. He, F. Li, and G. F. Chen, *Sci. Rep.* **2**, 389 (2012).
- <sup>11</sup>O. Gunnarsson, *Rev. Mod. Phys.* **69**, 575 (1997).
- <sup>12</sup>J. L. Janssen, M. Côté, S. G. Louie, and M. L. Cohen, *Phys. Rev. B* **81**, 073106 (2010).
- <sup>13</sup>C. Faber, J. L. Janssen, M. Côté, E. Runge, and X. Blase, *Phys. Rev. B* **84**, 155104 (2011).
- <sup>14</sup>T. Kato, T. Kambe, and Y. Kubozono, *Phys. Rev. Lett.* **107**, 077001 (2011).
- <sup>15</sup>A. Subedi and L. Boeri, *Phys. Rev. B* **84**, 020508(R) (2011).
- <sup>16</sup>M. Casula, M. Calandra, G. Profeta, and F. Mauri, *Phys. Rev. Lett.* **107**, 137006 (2011).
- <sup>17</sup>T. Kosugi, T. Miyake, S. Ishibashi, R. Arita, and H. Aoki, *J. Phys. Soc. Jpn.* **78**, 113704 (2009).
- <sup>18</sup>O. Gunnarsson and G. Zwirner, *Phys. Rev. Lett.* **69**, 957 (1992).
- <sup>19</sup>O. Gunnarsson, D. Rainer, and G. Zwirner, *Int. J. Mod. Phys. B* **6**, 3993 (1992).
- <sup>20</sup>V. P. Antropov, O. Gunnarsson, and A. I. Liechtenstein, *Phys. Rev. B* **48**, 7651 (1993).
- <sup>21</sup>The plot has been made with the Xcrysden plotting program; A. Kokalj, *J. Mol. Graphics Modell.* **17**, 176 (1999).
- <sup>22</sup>N. Marzari and D. Vanderbilt, *Phys. Rev. B* **56**, 12847 (1997).
- <sup>23</sup>In the text we prefer to give the definitions based on a finite summation over the BZ rather than the continuous limit of the integral, as in the practical implementation of the formula the finite grid is always used. This allows us to specify also the different  $k$  grids used for various quantities. In general, one can recover the continuous formulation by substituting  $\frac{1}{N_w} \sum_{\mathbf{k}}$  with  $\frac{V}{(2\pi)^3} \int_{\text{BZ}} d\mathbf{k}$ , whenever it appears.
- <sup>24</sup>F. Roth, M. Gatti, P. Cudazzo, M. Grobosch, B. Mahns, B. Bchner, A. Rubio, and M. Knupfer, *New J. Phys.* **12**, 103036 (2010).
- <sup>25</sup>I. Souza, N. Marzari, and D. Vanderbilt, *Phys. Rev. B* **65**, 035109 (2001).
- <sup>26</sup>P. Giannozzi, S. Baroni, N. Bonini, M. Calandra, R. Car, C. Cavazzoni, D. Ceresoli, G. L. Chiarotti, M. Cococcioni, I. Dabo *et al.*, *J. Phys.: Condens. Matter* **21**, 395502 (2009).
- <sup>27</sup>A. Mosto, J. R. Yates, Y.-S. Lee, I. Souza, D. Vanderbilt, and N. Marzari, *Comput. Phys. Commun.* **178**, 685 (2008).
- <sup>28</sup>P. B. Allen, *Phys. Rev. B* **6**, 2577 (1972).
- <sup>29</sup>W. L. McMillan, *Phys. Rev.* **167**, 331 (1968).
- <sup>30</sup>S. Baroni, S. de Gironcoli, A. Dal Corso, and P. Giannozzi, *Rev. Mod. Phys.* **73**, 515 (2001).
- <sup>31</sup>N. Marzari and D. Vanderbilt, *Phys. Rev. B* **56**, 12847 (1997).
- <sup>32</sup>M. Calandra, G. Profeta, and F. Mauri, *Phys. Rev. B* **82**, 165111 (2010).
- <sup>33</sup>F. Giustino, M. L. Cohen, and S. G. Louie, *Phys. Rev. B* **76**, 165108 (2007).
- <sup>34</sup>H. Okazaki, T. Wakita, T. Muro, Y. Kaji, X. Lee, H. Mitamura, N. Kawasaki, Y. Kubozono, Y. Yamanari, T. Kambe, T. Kato, M. Hirai, Y. Muraoka, and T. Yokoya, *Phys. Rev. B* **82**, 195114 (2010).
- <sup>35</sup>S. Ciuchi, R. C. Hatch, H. Hochst, C. Faber, X. Blase, and S. Fratini, *Phys. Rev. Lett.* **108**, 256401 (2012).
- <sup>36</sup>A. Devos and M. Lannoo, *Phys. Rev. B* **58**, 8236 (1998).
- <sup>37</sup>T. Kato, K. Yoshizawa, and K. Hirao, *J. Chem. Phys.* **116**, 3420 (2002).
- <sup>38</sup>M. Schlüter, M. Lannoo, M. Needels, G. A. Baraff, and D. Tománek, *Phys. Rev. Lett.* **68**, 526 (1992).
- <sup>39</sup>A. Devos and M. Lannoo, *Phys. Rev. B* **56**, 14703 (1997).

- <sup>40</sup>J. E. Han, O. Gunnarsson, and V. H. Crespi, *Phys. Rev. Lett.* **90**, 167006 (2003).
- <sup>41</sup>T. Kato and T. Yamabe, *J. Chem. Phys.* **117**, 2324 (2002).
- <sup>42</sup>T. Kato and T. Yamabe, *J. Chem. Phys.* **120**, 3311 (2004).
- <sup>43</sup>M. Lannoo, G. A. Baraff, M. Schlüter, and D. Tomanek, *Phys. Rev. B* **44**, 12106 (1991).
- <sup>44</sup>H. Fröhlich, *Adv. Phys.* **3**, 325 (1954).
- <sup>45</sup>G. Giovannetti and M. Capone, *Phys. Rev. B* **83**, 134508 (2011).
- <sup>46</sup>M. Kim, B. I. Min, G. Lee, H. J. Kwon, Y. M. Rhee, and J. H. Shim, *Phys. Rev. B* **83**, 214510 (2011).
- <sup>47</sup>Y. Nomura, K. Nakamura, and R. Arita, *Phys. Rev. B* **85**, 155452 (2012).